Acta Geophysica (2025) 73:1281–1295
https://doi.org/10.1007/s11600-024-01416-1

RESEARCH ARTICLE - APPLIED GEOPHYSICS

Petro-elastic model of the multiple pore-crack structure of carbonate rocks based on digital cores

Mengqiang Pang[1,5] · Jing Ba[1] · José M. Carcione[1,2] · Zhifang Yang[3,4] · Erik Saenger[5,6,7]

Received: 7 December 2023 / Accepted: 8 July 2024 / Published online: 22 July 2024

Abstract

Underground carbonate deposits are widespread worldwide and have considerable hydrocarbon potential. They are generally characterized by a complex microscopic structure that affects the properties of the macroscopic fluid flow and the relevant petrophysical behavior. In recent years, advances in digital technology have helped reveal the microstructures (i.e., pore connections, cracks, pore size and radius, etc.) of rocks in the subsurface. In this work, drill cores (cylinder) are taken from a deep carbonate deposit in the Sichuan Basin in western China to perform computed tomography (CT) scans, thin sections and mineral analysis. The characteristics of lithology and pore structure are investigated. Ultrasonic experiments with different fluid types and pressures are conducted to determine rock samples' wave velocities, attenuation and crack porosity. The experimental data show that the rocks have low porosity/permeability and a complex pore/crack system, leading to significant pressure, crack and fluid type effects on the velocities, dispersion and attenuation. We develop a model of multiple pore-crack structures for carbonates by considering the complex structure and fluid properties. Digital cores are reconstructed based on CT scans, image processing and threshold segmentation. The aspect ratios of pores and cracks are extracted with their volume fractions to simulate the rock skeleton with the differential effective medium theory. The Biot–Rayleigh wave propagation equations are applied to simulate the effects of different pore and fluid types on the velocity and attenuation of P-waves. The agreement between the modeling results and the ultrasonic and log data confirms that the model can validly reproduce the wave responses.

Keywords Carbonate · Pore structure · Digital core · Rock-physics modeling · Attenuation

Edited by Prof. Qamar Yasin (ASSOCIATE EDITOR) / Prof. Gabriela Fernández Viejo (CO-EDITOR-IN-CHIEF).

✉ Jing Ba
jba@hhu.edu.cn

1 School of Earth Sciences and Engineering, Hohai University, Nanjing 211100, China

2 National Institute of Oceanography and Applied Geophysics–OGS, 34010 Trieste, Italy

3 Research Institute of Petroleum Exploration and Development, PetroChina, Beijing 100083, China

4 China National Petroleum Corporation Key Laboratory of Geophysics, Beijing 100083, China

5 Hochschule Bochum, Am Hochschulcampus 1, 44801 Bochum, Germany

6 Fraunhofer IEG - Institution for Energy Infrastructures and Geothermal Energy, Am Hochschulcampus 1, 44801 Bochum, Germany

7 Institute of Geology, Mineralogy, and Geophysics, Ruhr-University Bochum, Universitätsstrasse 150, 44801 Bochum, Germany

Introduction

As the global demand for hydrocarbon resources continues to increase and conventional oil and gas reserves are gradually depleted, the development of deep hydrocarbon reservoirs, combined with technological advances to date, has become a significant source (and challenge) for the petroleum industry (Zou et al. 2014; Wang et al. 2020; Pang et al. 2020; Ablimiti et al. 2022; Jun et al. 2023). The Longwangmiao Formation in the central Sichuan Basin in western China comprises carbonate reservoirs at a depth of more than 4.5 km, rich in natural gas reserves (Zhou et al. 2015; Pang et al. 2019). The reservoirs are characterized by complicated microporous structures, pores, caves and cracks as well as the heterogeneous distribution of immiscible fluids (Pang et al. 2019), which affect the macroscopic responses and acoustic properties (Guo et al. 2020a, 2020b; Zhang et al. 2021, 2022; Pang et al. 2024a; Luo et al. 2023; Li et al. 2024).

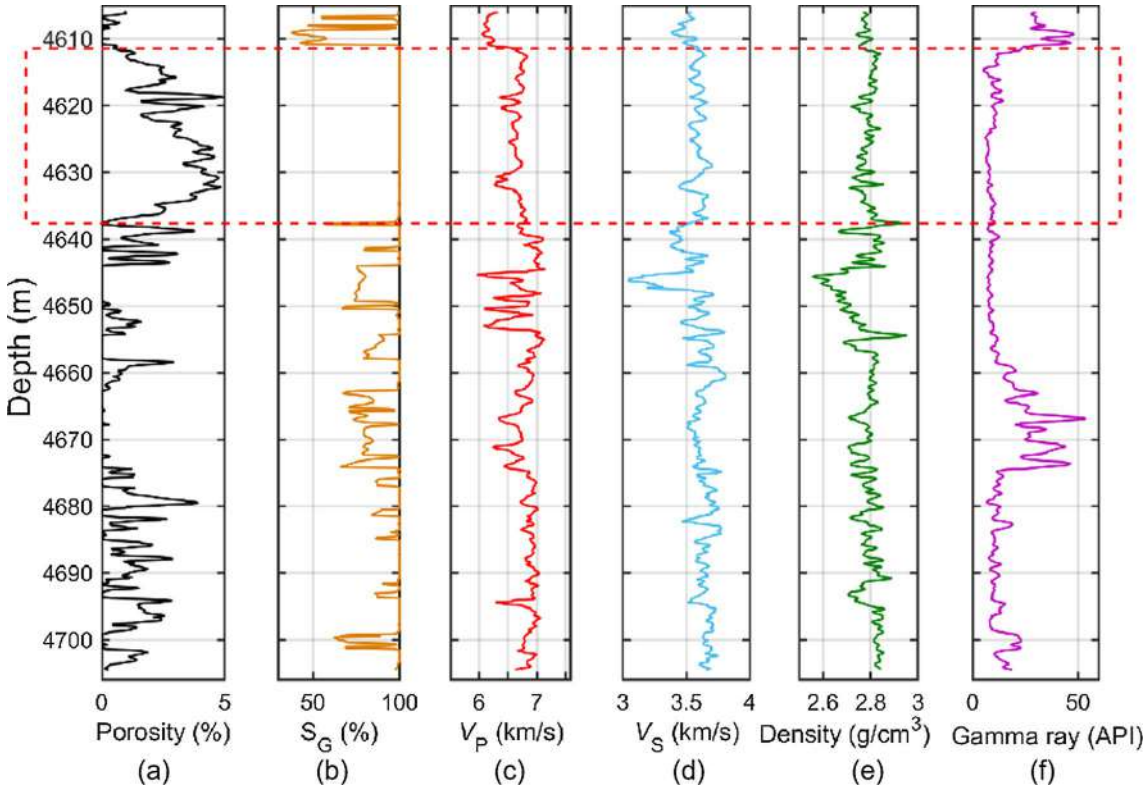

Fig. 1 Log data from Well A. Left to right: **a** Porosity, **b** gas saturation, **c** *P*-wave velocity, **d** *S*-wave velocity, **e** density and **f** gamma-ray

Experimental and theoretical studies have shown that the wave velocities and attenuation are related to the pore structure, the type of fluid and the saturation in the rock (Sakhaee-Pour and Bryant 2014; Solano et al. 2017; Ba et al. 2017; Kumar et al. 2019; Ghasemi et al. 2020). The wave-induced local fluid flow within the pore system is a critical factor leading to the velocity dispersion and attenuation. Theoretical models have been developed to interpret the relationships between pore structure, fluid distribution, wave velocity and anelasticity, including patchy saturation models (White 1975; Carcione et al. 2003; Vogelaar et al. 2010; Kobayashi and Mavko 2016), double-porosity models (Pride and Berryman 2003; Tang 2011; Ba et al. 2011) and squirt-flow models (Dvorkin and Nur 1993; Chapman 2003; Gurevich et al. 2010; Song et al. 2016).

Recently, the characterization of microstructure and fluid distribution based on rock-physics models (RPMs) has attracted widespread attention (Carcione and Avseth 2015; Pang et al. 2022, 2024b), which simulates the reservoir with a simplified pore structure by assuming that the rock contains one or two types of pores with single shapes (Gupta et al. 2012; Golikov et al. 2012; Ba et al. 2013; Tan et al. 2020; Pang et al. 2020, 2021). However, for the carbonate reservoirs of the Sichuan Basin, the simplified geometries of the assumptions cause difficulties in describing the complex pore structure.

With the advances in X-ray computed tomography (CT), digital core technology has become an important approach for the study of rock microstructures and pore fluid distribution (Okabe and Blunt 2004; Andrä et al. 2013; Kadyrov et al. 2022). The method maps the minerals as well as the geometric and volumetric properties of the rock on the location-dependent volume (Wildenschild et al. 2002; Zhou et al. 2016; Schlüeter et al. 2014; Alqahtani et al. 2021). The digital rocks are reconstructed by numerical processing of images to reveal the geometric and topological structures of pores and throats (Madonna et al. 2013; Sun et al. 2019), porosities and permeabilities associated with multiphase flow (Bultreys et al. 2022; Spurin et al. 2023) and capillary pressure (Paustian et al. 2021), in areas such as hydrogen storage (Jangda et al. 2023), general upscaling problems (Menke et al. 2021), effective elastic and hydraulic properties and thermal conductivity (Saenger et al. 2005, 2016; Saxena et al. 2019; Siegert et al. 2022; Wang et al. 2022).

This work uses digital cores to obtain information about the microstructures and suitable RPM. Core samples are collected from the carbonate reservoirs in working area G of Sichuan Basin to perform CT scanning, mineral analysis and cast thin-section analysis (CTS) to analyze the pore-throat system. *P*- and *S*-wave ultrasonic experiments related to different fluid types, and confining pressures are performed to study the effects of lithology, pressure, cracks and fluid

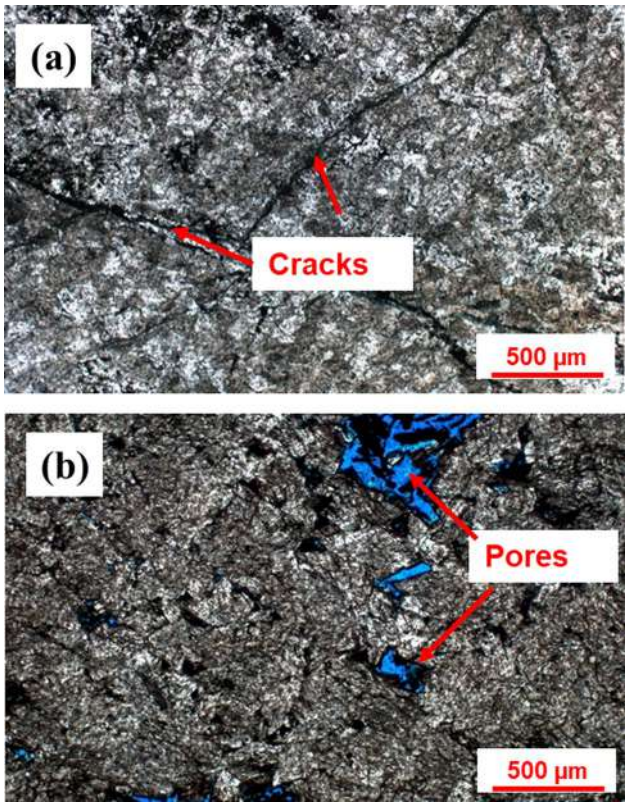

Fig. 2 Cast thin sections of the carbonate samples DS3 (**a**) and DS17 (**b**)

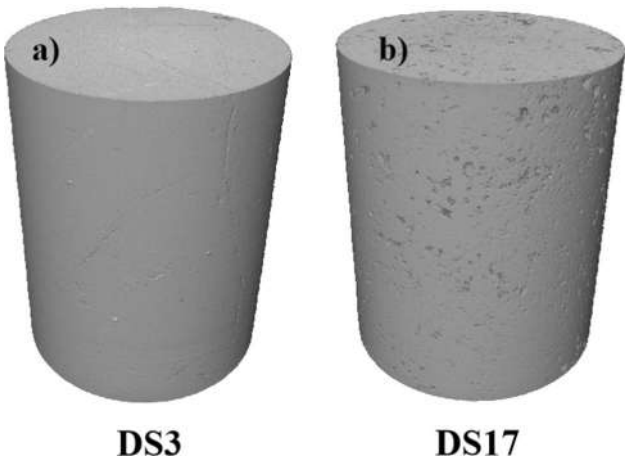

Fig. 3 Three-dimensional CT images of samples DS3 (**a**) and DS17 (**b**)

on velocities and attenuation. We propose a multiple pore-crack structure model (MPCSM) based on the digital core method and the equivalent medium and wave propagation equations. The wave velocities and attenuation for different fluid types (gas/water) in the real pore space are modeled and compared with the measured data of the sample and the actual field data.

Core samples and laboratory experiments

Geology and cores

The working area comprises the carbonate formations with hydrocarbon resources in the Sichuan Basin's working area. The depth of the Longwangmiao Formation reservoirs is more than 4.5 km, the temperature is about 120 °C and the overburden and pore pressures are about 110 MPa and 65–70 MPa, respectively. The rocks have a complex pore structure and an immiscible fluid mixture of gas and water; lithologically, it comprises dolomite rock with low porosity, and the pore fluids are mainly gas and water (Zhou et al. 2015; Qu et al. 2023). Petrophysical analyses allow it to evaluate logging data properties (Well A). The porosity, gas saturation, *P*- and *S*-wave velocities, density and natural gamma of the well log are giving (Fig. 1), with the red dashed box indicating the section of the formation with high gas production. Reservoir porosity is low (less than 5%), gas saturation is greater than 30%, elastic velocities and density are high and natural gamma is low.

We take two cores (DS3 and DS17) from Well A high gas production section at a depth of 4627.15 m and 4625.6 m, respectively. DS3 and DS17 are processed into cylinders with a diameter of 38 mm and a length of about 50 mm, with porosities of 1.96% and 3.46%, permeabilities of 0.16 and 0.001 mD and densities of 2.802 and 2.748 g/cm^3, respectively. The samples were subjected to CTS and CT scan tests and P- and S-wave ultrasonic experiments in dry and water-saturated conditions and at different pressures to analyze the petrophysical responses.

Thin sections and CT scans

Figure 2 shows the CTS of the samples, with DS3 developed cracks and DS17 containing intergranular and dissolved pores. The mineral analyses by X-ray diffraction (XRD) experiment show that the samples are almost pure dolomite with a content of more than 98%. CT scans carry on the samples to obtain the 3D scan data of DS3 and DS17 (Fig. 3). They contain 1980 and 1954 images of 1398×1404 and 1408×1402 pixels, respectively, and a resolution of 27.6 μm per pixel. The CT datasets have a 16-bit format, resulting in a grayscale intensity ranging from 0 to 65,535, reflecting the pore-throat spaces and minerals. It shows that DS3 is denser than DS17, with a lower pore content, but contains cracks, consistent with the results of the thin section and porosity measurements.

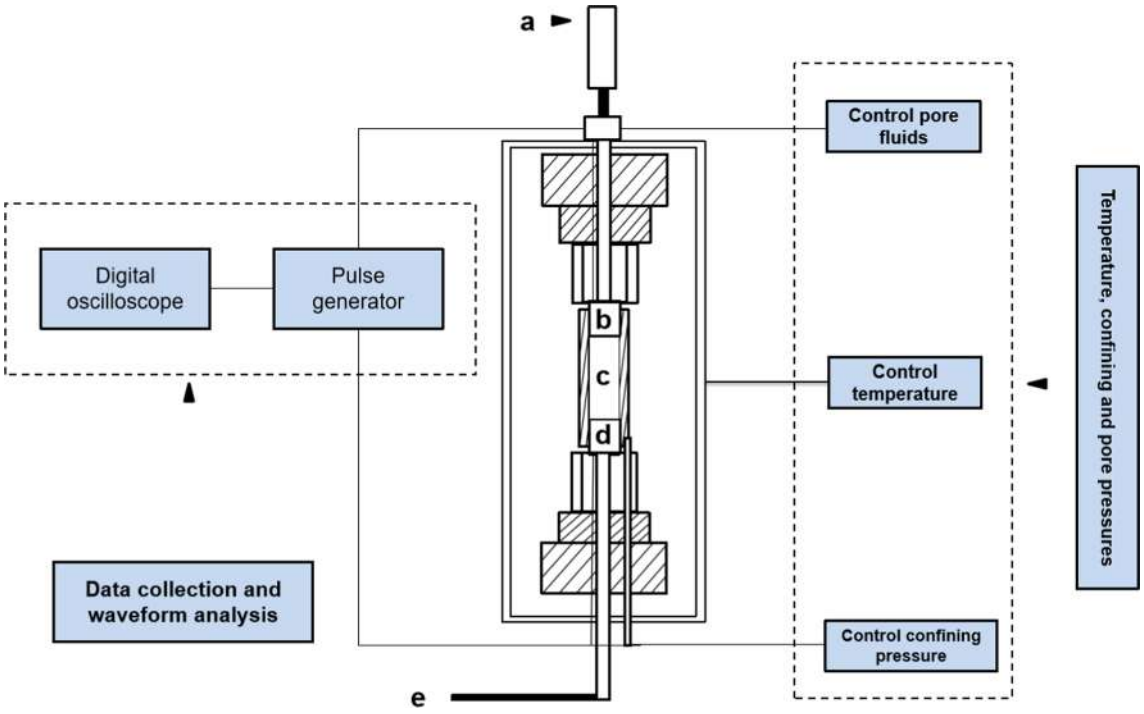

Fig. 4 Diagram of the ultrasonic experimental setup. **a** Pore fluid inlet; **b** wave transmitter; **c** rock sample; **d** receiving transducer and **e** pore fluid outlet

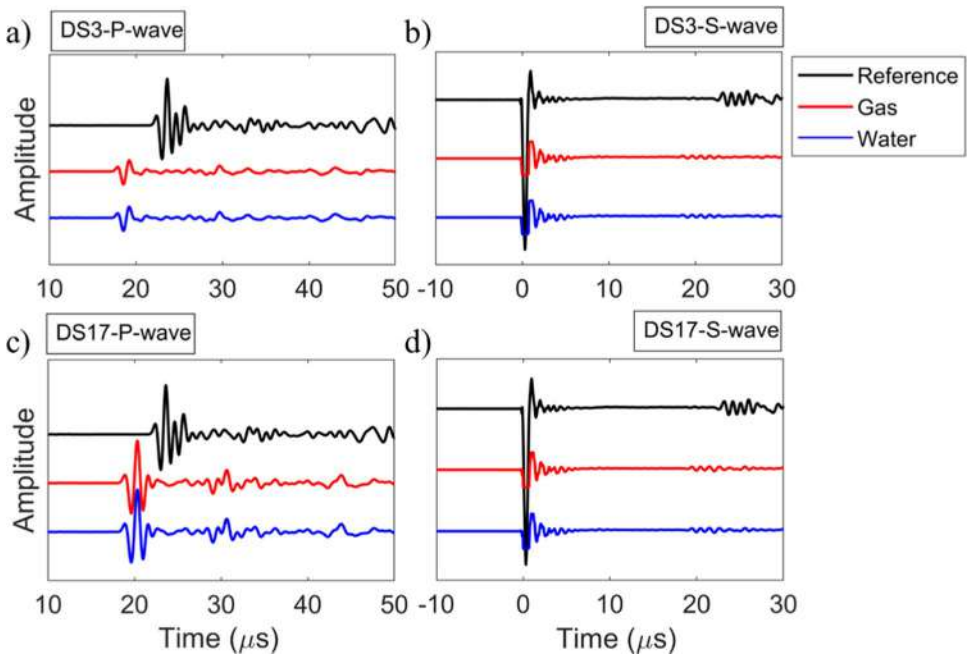

Fig. 5 Ultrasonic waveforms of rock samples and reference material (**a** *P*-wave of DS3; **b** *S*-wave of DS3; **c** *P*-wave of DS17 and **d** *S*-wave of DS17). The red and blue lines represent full gas and full water saturation states, and the black line represents the reference material

Ultrasonic measurements

P- and *S*-wave ultrasound investigations are carried out with different confining pressures and fluid types. First, the rock is dried and placed in the experimental setup (Fig. 4), which consists of a digital oscilloscope and a pulse generator (Guo et al. 2009), with *P* and *S* waves generated by the wave transmitter (b) on steel endplates; the receiving transducer (d) is connected to the digitizing board in the PC via a signal

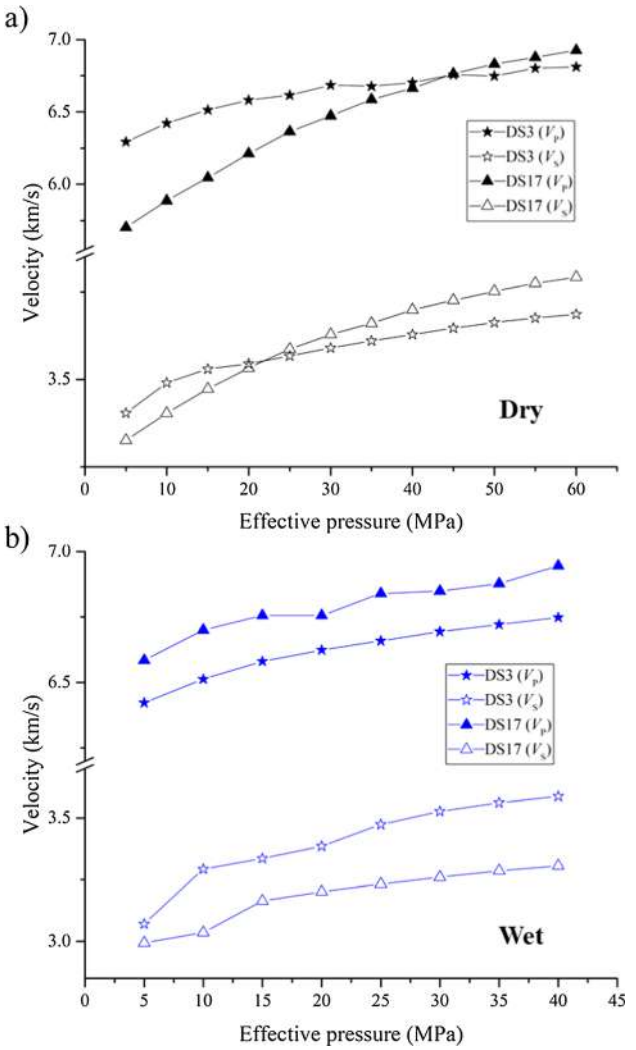

Fig. 6 *P*- and *S*-wave velocities of the samples as a function of effective pressure, **a** dry case and **b** wet case

amplifier; the pore fluid inlet (a) and outlet (e) in endplate allow the passage of pore fluids through the sample (c). Ultrasonic measurements (1 MHz) are performed at confining pressures of 5, 10, 15, 20, 25, 30, 35, 40, 45, 50, 55 and 60 MPa, pore pressure of one atmosphere and a temperature of 26.5 °C to record the waveforms (Fig. 5). Then, water is injected into the samples at a pore pressure of 20 MPa, and the waveforms are recorded at confining pressures of 25, 30, 35, 40, 45, 50, 55 and 60 MPa (Fig. 5). In addition, aluminum blocks of the same size as the samples are prepared as reference material, and the waveforms are also measured.

Elastic wave velocities are obtained on the basis of the sample length and the propagation time, resulting from the first arrivals of the waveforms at different pressures. The attenuation (reciprocal of the quality factor, 1/*Q*) of the specimens is computed with the spectral ratio method (Toksöz et al. 1979) as follows:

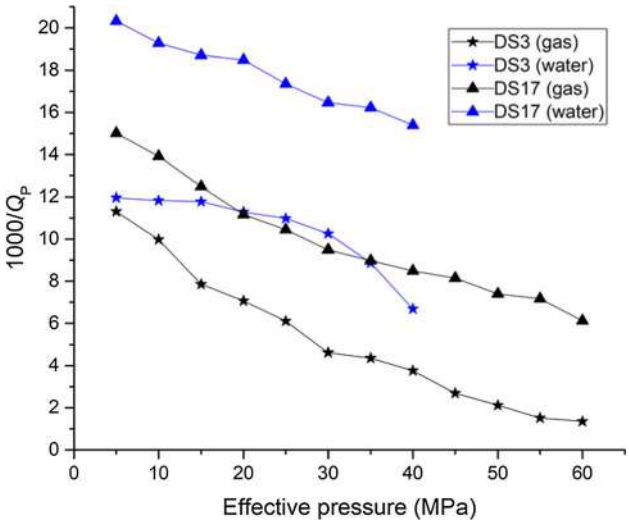

Fig. 7 *P*-wave attenuation of the samples as a function of the effective pressure in the dry (gas) and wet (water) states

$$\ln\left[\frac{A_1(f)}{A_2(f)}\right] = -\frac{\pi x}{QV}f + \ln\left[\frac{G_1(f)}{G_2(f)}\right], \quad (1)$$

where f is the frequency, and $A_1(f)$ and $A_2(f)$ are the amplitude spectra of the rock and reference material, respectively. $G_1(f)$ and $G_2(f)$ are geometrical factor related to the shape and size of the sample and aluminum block, x is the sample length and V denotes the wave velocity.

Experimental results

Figures 6 and 7 show the experimental results of the two samples, with the *P*- and *S*-wave velocities (V_P and V_S) and the *P*-wave attenuation as a function of the effective pressure (P_{eff}, confining minus pore pressure) for the gas (black) and water-saturated (blue) cases. The scatters represent different samples. The elastic wave velocities increase, and the attenuation decreases with increasing P_{eff}, which is mainly related to gradual closing cracks with increasing P_{eff}.

Furthermore, the *P*-wave attenuation of rock at full water saturation is higher than that of gas-saturated rock, and the attenuation of DS17 is higher than that of DS3. In the dry state, the wave velocities of DS17 in the low-pressure range are lower than those of DS3, while the behavior reverses with increasing P_{eff}. In the wet case, DS17 has a lower V_S and a higher V_P than DS3. The waves induce a local fluid flow in the pore space, which causes wave dissipation. Sample DS17, with a higher porosity and more pore fluid, attenuates more than DS3 (Fig. 7).

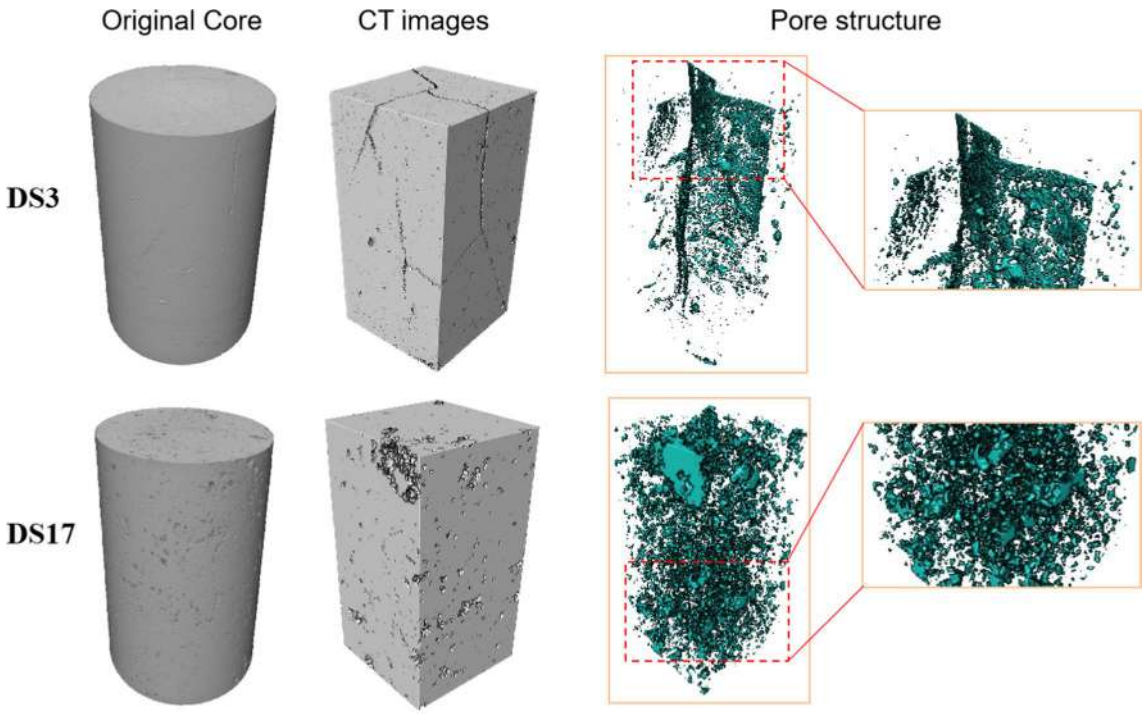

Fig. 8 CT scan images and pore structure of carbonate samples (DS3 and DS17)

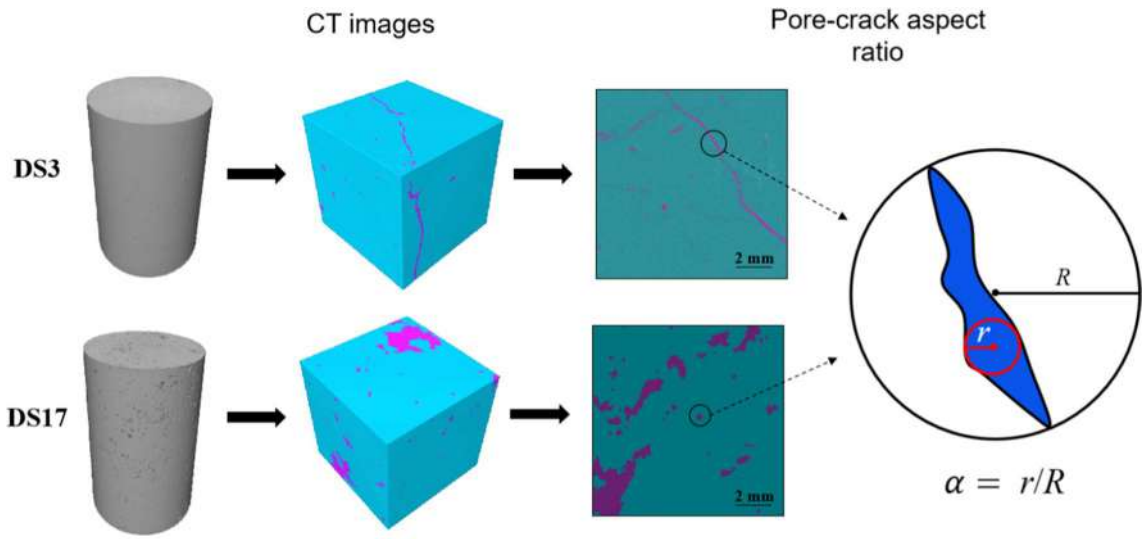

Fig. 9 Estimation flowchart of the pore-crack aspect ratios of the samples

Estimation of the pore structure

We reconstruct digital 3D cores based on the CT images and CTS to investigate the pore-crack structures of the carbonates. Subsequently, we obtain effective crack density and aspect ratio based on the experimental data at different pressures and David–Zimmerman (DZ) model (David and Zimmerman 2012) to calculate crack porosity of the samples, which is used to quantitatively characterize the effects of cracks on velocity and attenuation.

Digital cores

First, three-dimensional digital kernels are constructed from rock images, a non-local-mean filter is applied for denoising

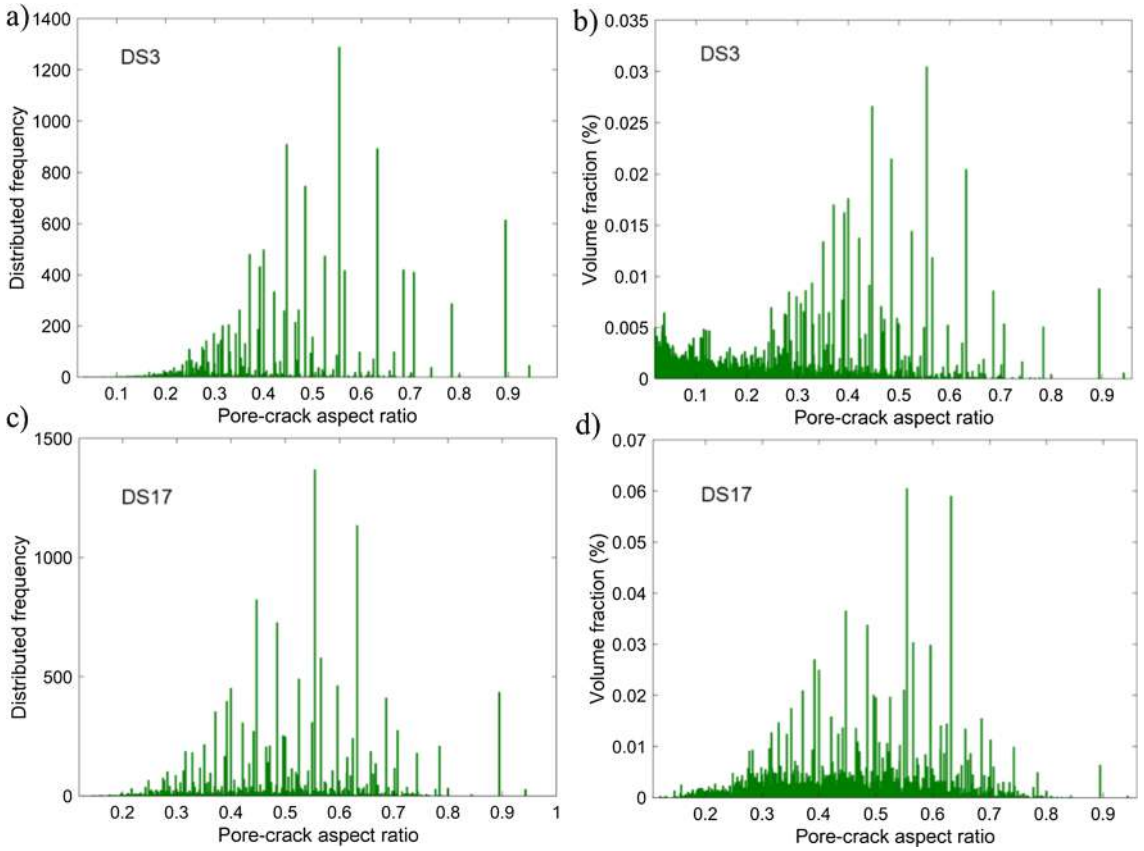

Fig. 10 Distributed frequency and volume fraction as a function of the pore-crack aspect ratios of samples DS3 (a and b) and DS17 (c and d), respectively

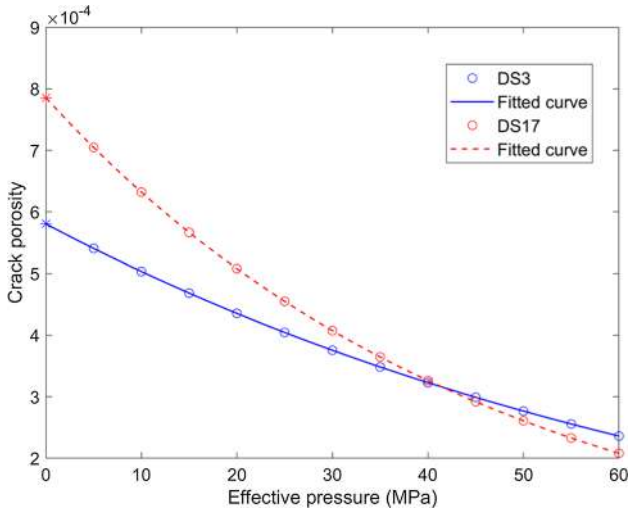

Fig. 11 Crack porosity of the samples as a function of effective pressure

and threshold segmentation. The pixels of the dataset represent the pore space and minerals (Fig. 8). It shows the samples, CT images and the pore structure in 3D space. Subsequently, the representative elemental volume (REV) is selected to obtain an appropriate size that can accurately characterize the rock microstructure while meeting storage and computational requirements. In addition to meeting these two conditions, the results of porosity are also used as constraint conditions to obtain the appropriate REV. Due to the limited calculation capabilities, a partial volume of 400^3 pixels is selected from the individual 3D dataset. It is considered that REV can be adopted in the analyses on acoustic characteristics of rock (Saxena et al. 2019; Kadyrov et al. 2022).

Then, the micropore structure is characterized based on the digital samples. Figure 9 shows a flowchart for the calculation of the pore-crack aspect ratios of the samples. First, based on the segmented samples, the pixel labeling algorithm of connecting area is used to label all the connected pores in the images. The radii (r, R) of the minor and major axes of the labeled pores are calculated by using the maximum inner tangent and minimum outer circle algorithms, respectively. Finally, the different pore-crack aspect ratios (the ratio of the radii of the minor and major axes, r/R) and the corresponding volume fractions (the proportion of pixels representing the pores) are determined (Fig. 10). From the

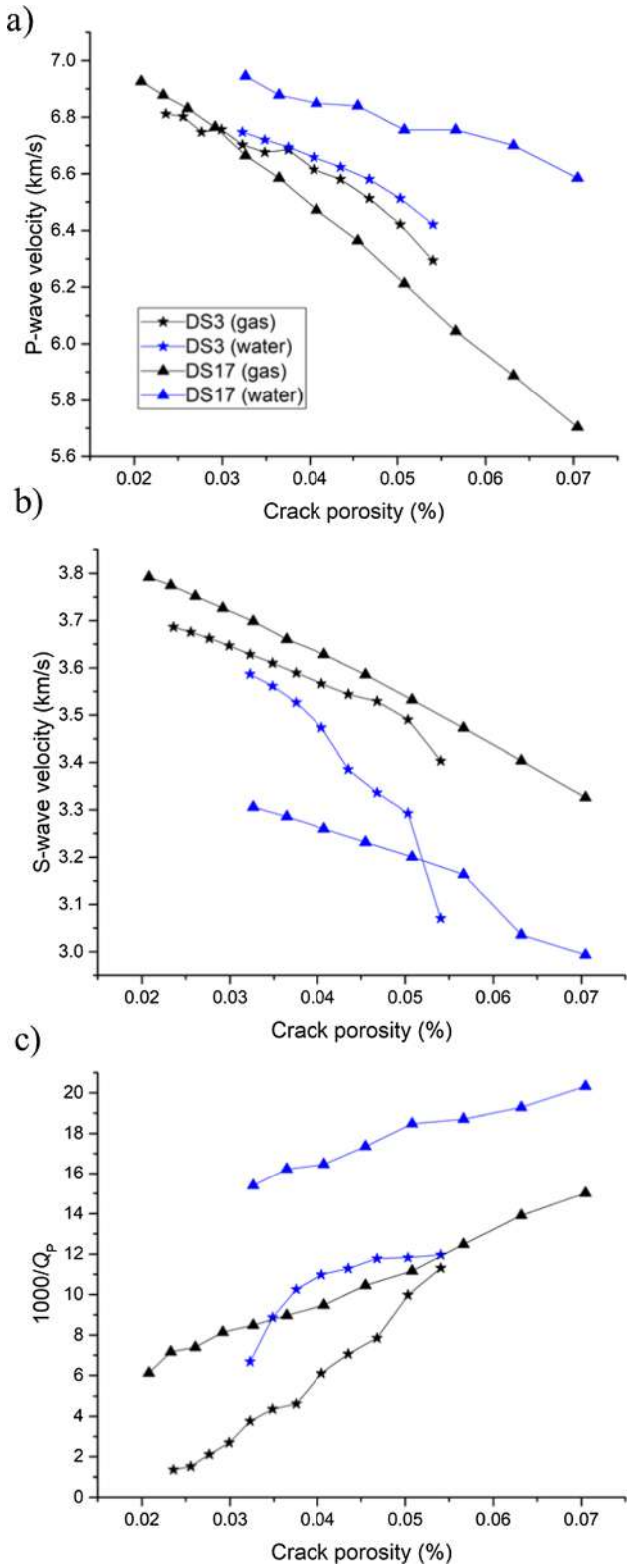

Fig. 12 **a** *P*- and **b** *S*-wave velocities, and **c** *P*-wave attenation as a function of crack porosity

figure, the aspect ratio distribution essentially corresponds to the Gaussian distribution, and sample DS3 shows many micropores in the region with small aspect ratios.

Estimation of crack porosity

We estimate the crack porosity of rocks based on the experimental data by using the DZ model. The soft pores internal the rock are assumed to be closed at the high-pressure limit, where the total porosity approaches the stiff porosity well (David and Zimmerman 2012; Qi et al. 2021). First, the rocks' bulk and shear moduli are estimated from the elastic wave velocities at high effective pressures. The elastic moduli are given based on the Mori–Tanaka theory (Mori and Tanaka et al. 1973):

$$K_{\text{stiff}} = K_0 \Big/ \left(1 + \frac{\phi_{\text{stiff}}}{1-\phi_{\text{stiff}}} P\right), \tag{2}$$

$$G_{\text{stiff}} = G_0 \Big/ \left(1 + \frac{\phi_{\text{stiff}}}{1-\phi_{\text{stiff}}} Q\right), \tag{3}$$

where K_{stiff} and G_{stiff} are the bulk and shear moduli, respectively, of the rock containing only stiff pores, K_0 and G_0 are the corresponding moduli of grain, ϕ_{stiff} is the stiff porosity and P and Q are polarization factors, which are related to the aspect ratio α of the pores and Poisson's ratio v of the solid (Zhang et al. 2019; Qi et al. 2021).

Next, the effects of cracks on the elastic properties of rock are considered, and the effective moduli are:

$$K_{\text{eff}} = K_{\text{stiff}} \Big/ \left(1 + \frac{16\left(1-\left(v_{\text{stiff}}\right)^2\right)\Gamma}{9\left(1-2v_{\text{stiff}}\right)}\right), \tag{4}$$

$$G_{\text{eff}} = G_{\text{stiff}} \Big/ \left(1 + \frac{32\left(1-v_{\text{stiff}}\right)\left(5-v_{\text{stiff}}\right)\Gamma}{45\left(2-v_{\text{stiff}}\right)}\right), \tag{5}$$

where $v_{\text{stiff}}=(3K_{\text{stiff}} - 2G_{\text{stiff}})/(6K_{\text{stiff}} + 2G_{\text{stiff}})$ is the Poisson ratio of the rock containing only stiff pores. The least squares regression fits the cumulative crack density Γ at each effective pressure.

Furthermore, the pore aspect ratio α_{p} as a function of effective pressure is as follows (Zhang et al. 2019):

$$\alpha_{\text{p}} = \frac{4\left[1-\left(v_{\text{eff,}}\right)^2\right]P_{\text{eff}}}{\pi E_{\text{eff}}}, \tag{6}$$

where the effective Young's modulus at high pressures is $E_{\text{eff}} = 3K_{\text{eff}}[1-2v_{\text{eff}}]$.

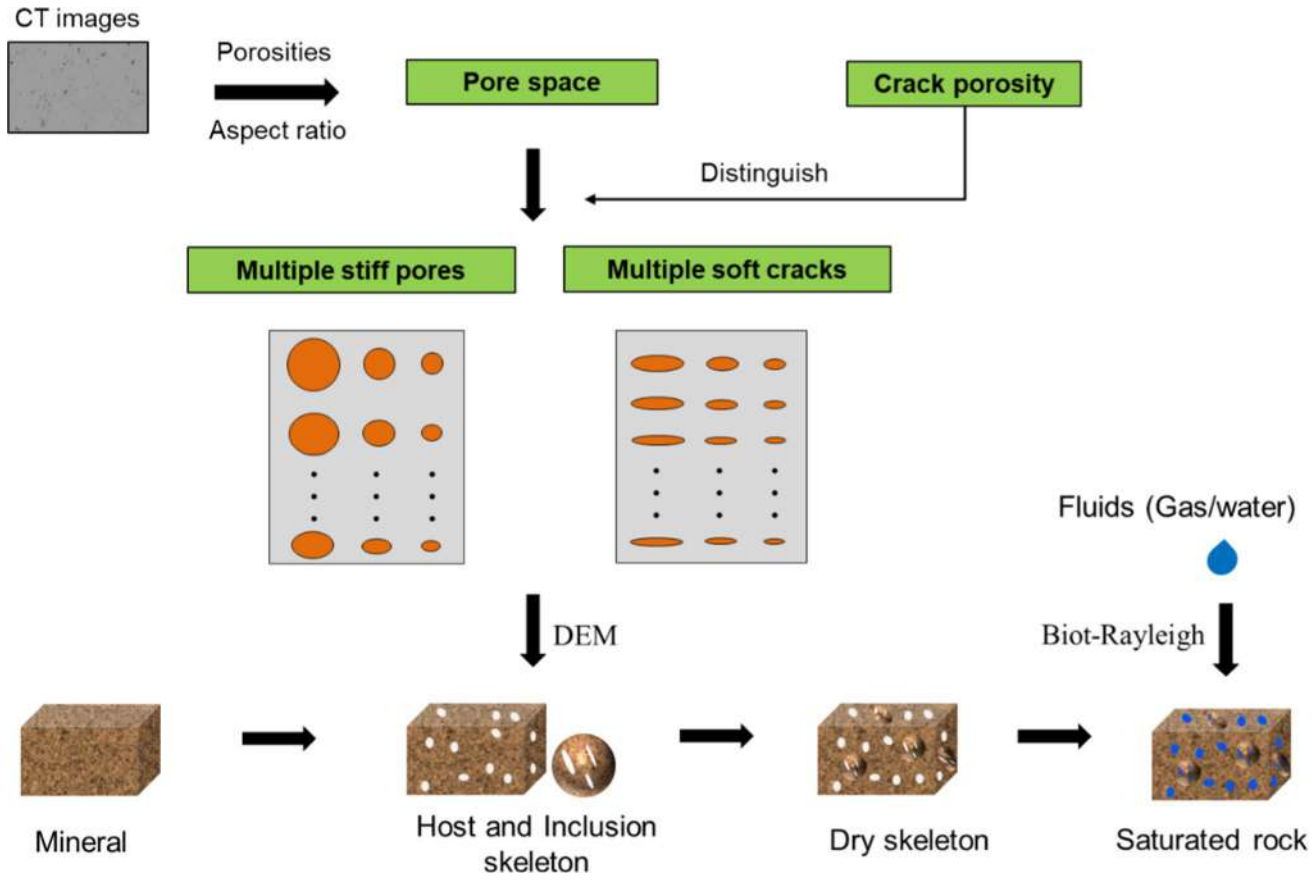

Fig. 13 Flowchart of the MPCSM

The crack porosity ϕ_C can be determined as follows (David and Zimmerman 2012):

$$\phi_C = \frac{4\pi\alpha_p}{3}\Gamma. \tag{7}$$

Figure 11 shows the estimated results, where ϕ_C decreases with P_{eff}. At low pressures, ϕ_C of sample DS17 is higher than that of DS3, while ϕ_C of DS3 is higher than that of DS17 when P_{eff} increases, indicating that more micropores of DS17 are gradually closed with increasing P_{eff}, which is consistent with the results in Fig. 6.

Figure 12 shows the elastic velocities and *P*-wave attenuation as a function of ϕ_C, where the velocities decrease with ϕ_C, while the attenuation increases. The wet-rock samples have a higher V_P and a lower V_S compared to dry ones. Sample DS17 exhibits a greater difference in elastic velocities and attenuation between the two saturation states, which is consistent with the greater dispersion and attenuation observed in Figs. 6 and 7.

Multiple pore-crack model

Based on the digital core method and the theories of equivalent medium and wave propagation, we propose a multiple pore-crack structure model (MPCSM) for carbonate rocks with complex pore structures and fluid mixture, which is shown in Fig. 13 as a flowchart of modeling. By considering a variety of pores and cracks with different aspect ratios in the rocks, the model addresses the limitations of conventional models that rely on the simplified assumptions of rock microstructures and mitigates to some extent the effects of the complex geometry of carbonate rocks.

Modeling procedure

For the carbonate reservoirs, the pore space is extracted based on digital cores, divided into several stiff and soft pores with different aspect ratios according to the crack porosity (Fig. 13). Next, we consider a double-porosity structural model, assuming that the rock skeleton consists of a host medium and an inclusion phase containing the

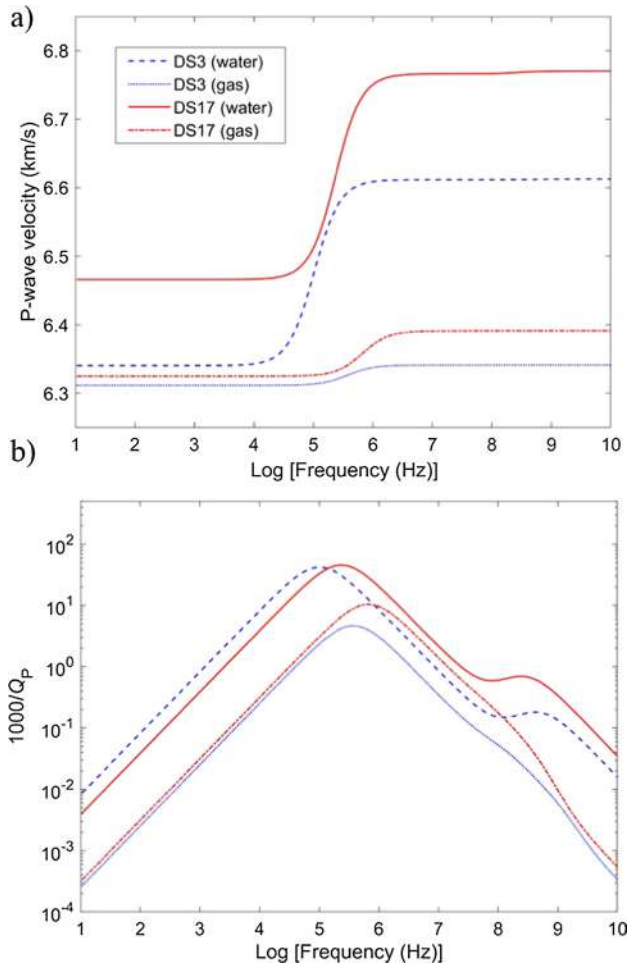

Fig. 14 **a** *P*-wave velocity and **b** attenuation of the carbonate samples at full gas and water saturations as a function of frequency

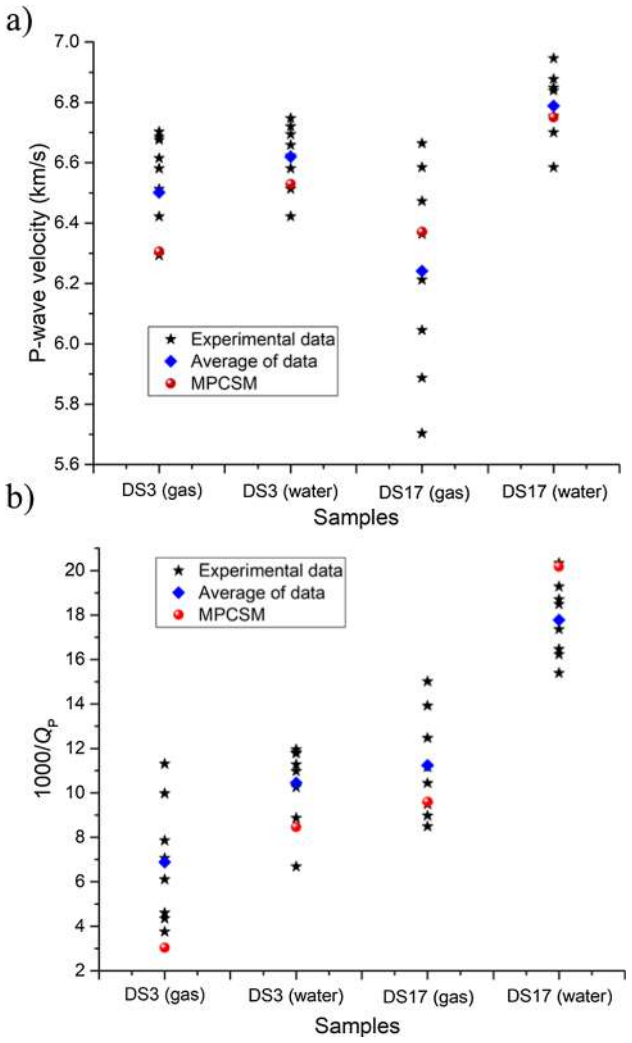

Fig. 15 Comparison between the MPCSM results (**a** *P*-wave velocity and **b** attenuation) and experimental data

same mineral. The host medium and inclusion phase contain stiff and soft pores, respectively, with different aspect ratios. The differential effective medium theory—DEM (Berryman 1992) is applied to add the multiple pores and cracks into the host medium and inclusions, respectively, and then add the inclusions into the host phase to obtain the elastic moduli of the dry rock. Berryman (1992) proposed the DEM equations to compute the bulk and shear moduli of the host, inclusion and rock skeleton:

$$(K_2 - K^*)P^{(*2)}(y) = (1-y)\frac{\mathrm{d}}{\mathrm{d}y}[K^*(y)], \tag{8}$$

$$(\mu_2 - \mu^*)Q^{(*2)}(y) = (1-y)\frac{\mathrm{d}}{\mathrm{d}y}[\mu^*(y)], \tag{9}$$

where the initial conditions are $K^*(0) = K_1$ and $\mu^*(0) = \mu_1$, i.e., the bulk and shear moduli of the host, respectively, y is the content of phase 2, K_2 and μ_2 are the corresponding moduli and P^{*2} and $Q^{*2}$are geometrical factors (Mavko et al. 2009).

The Biot–Rayleigh equations (Ba et al. 2011, Appendix A) give the wet-rock moduli, and the velocities and attenuation of rocks containing multiple pores/cracks, and the MPCSM is constructed to model the wave responses. *P*-wave velocity and attenuation are obtained from a plane wave analysis (Carcione 2022):

$$V_{\mathrm{P}} = \left[\mathrm{Re}\left(v^{-1}\right)\right]^{-1}, \tag{10}$$

$$Q^{-1} = \frac{\mathrm{Im}\left(v^2\right)}{\mathrm{Re}\left(v^2\right)}, \tag{11}$$

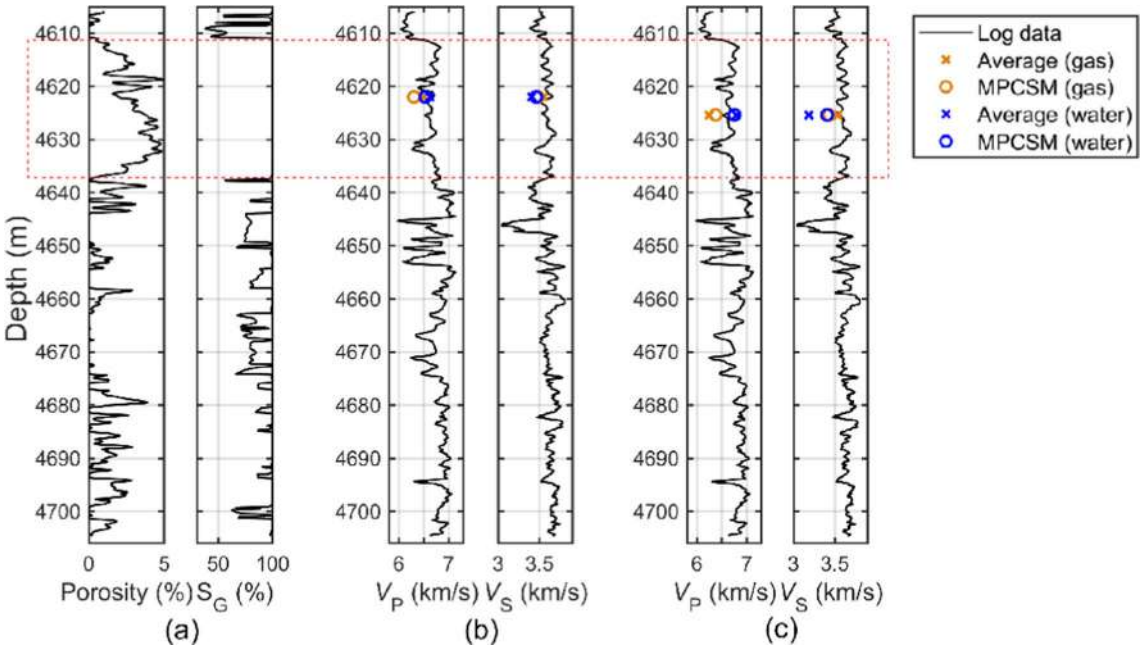

Fig. 16 Modeling results compared with the ultrasonic and log data (**a** porosity and gas saturation; **b** results and data of DS3 and **c** results and data of DS17). The circles and crosses represent the model results and the average values of the experimental data, respectively

with the complex velocity $v = \omega/k$ (Appendix A), while ω and k being the angular frequency and complex wavenumber, respectively.

Model responses

The established model is applied to simulate the wave responses of the carbonate samples with different fluids. According to Mavko et al. (2009), the dolomite has bulk, shear moduli and density of 94.9 and 45 GPa, and 2.87 g/cm^3, respectively. As for the properties of gas and water, the bulk modulus, density and viscosity coefficient are 0.018 and 2.24 GPa, 0.09 and 1.002 g/cm^3 and 1.6×10^5 and 9.8×10^4 Pa s, respectively. The aspect ratios of pores and cracks and the corresponding volume fractions (Fig. 10) are determined by using the digital cores, and the radius R_0, porosity ϕ_{20} and aspect ratio of the inclusion are 10 μm, 0.2 and 1, respectively.

The *P*-wave velocity dispersion and attenuation are simulated for the cases of gas and water saturation (Fig. 14). The model results indicate that the dispersion and attenuation of the rock saturated with water are higher compared to rocks saturated with gas, and the main anelasticity bands are at a lower frequency. The *P*-wave velocity of DS3 is lower than that of DS17.

Model and data

The experimental data of the samples at different pressures are used to verify the model, Fig. 15 shows the *P*-wave velocity and the attenuation of the model at 1 MHz compared with the data. The mean values of the data are considered to check the velocity dispersion in the two saturation states. The sample DS17 with higher porosity shows a high dispersion. From Fig. 15, the model can effectively describe the dispersion of wave velocity and attenuation associated with the pore fluid.

To validate the model, log data from borehole A of the target formation (the red dashed box indicates the section with high gas production) are then extracted, together with the experimental samples at the sampling depth, (Fig. 16), with the black curves representing the log data. Figure 16a shows the porosity and gas saturation. The simulations (circles) and the average values of the ultrasonic data (crosses) are placed at the extraction depth (Fig. 16b and c represent DS3 and DS17, respectively), with yellow and blue representing gas and water saturation cases, respectively. Upon comparing the model results with the available data, it is observed that the simulations are generally consistent with the data. The deep burial depth and high overburden pressure (about 110 MPa) of the formation lead to higher elastic velocities than those in the measurements and simulations, except for sample DS17 with saturating water (which shows high-velocity dispersion, as described in Fig. 15).

Conclusions

In this study, rock cores were taken from carbonate reservoirs, and CT scans, XRD mineral analysis and thin sections were made to investigate the lithology, pores, throats and microstructures. Digital core samples are created using image processing algorithms to determine the aspect ratios of all pores and cracks and the corresponding volume fractions. Then, ultrasonic *P* and *S* experiments are performed at different pressures with full gas/water states. The crack porosity and attenuation are estimated by using the DZ model and the spectral ratio method, respectively. The pore structure and fluid type effects on the elastic properties are analyzed, finding that the cracks (associated with pressure) and pore fluid significantly affect the velocity and attenuation.

The proposal model considers the complex pore structures and fluid types for the structure of multiple pores and cracks. The model is built based on digital cores, DEM and the Biot–Rayleigh equations to obtain the wet-rock responses, compared with the ultrasonic and log data (Well A). The results show that the model can effectively describe the characteristics of wave dispersion and attenuation for the real microstructures with different saturating fluid types. This study bridges the gap between the digital core method and theoretical petrophysical modeling, which can be helpful for better understanding the fluid flow and mechanical behaviors of reservoirs with complex microstructures.

Appendix A

Biot–Rayleigh dispersion equation

The stiffness moduli of the wet rock as well as the velocity and attenuation of the *P*-waves are determined by using the Biot–Rayleigh equations (Ba et al. 2011). The complex wavenumber k is determined by inserting a plane *P*-wave kernel into the equations and solving the dispersion equation of:

$$\begin{vmatrix} a_{11}k^2+b_{11} & a_{12}k^2+b_{12} & a_{13}k^2+b_{13} \\ a_{21}k^2+b_{21} & a_{22}k^2+b_{22} & a_{23}k^2+b_{23} \\ a_{31}k^2+b_{31} & a_{32}k^2+b_{32} & a_{33}k^2+b_{33} \end{vmatrix} = 0, \tag{A-1}$$

where:

$$\begin{aligned}
&a_{11}=A+2N+\mathrm{i}(Q_2\phi_1-Q_1\phi_2)x_1\ b_{11}=-\rho_{11}\omega^2+\mathrm{i}\omega(b_1+b_2),\\
&a_{12}=Q_1+\mathrm{i}(Q_2\phi_1-Q_1\phi_2)x_2\ b_{12}=-\rho_{12}\omega^2-\mathrm{i}\omega b_1,\\
&a_{13}=Q_2+\mathrm{i}(Q_2\phi_1-Q_1\phi_2)x_3\ b_{13}=-\rho_{13}\omega^2-\mathrm{i}\omega b_2,\\
&a_{21}=Q_1-\mathrm{i}R_1\phi_2x_1\ b_{21}=-\rho_{12}\omega^2-\mathrm{i}\omega b_1,\\
&a_{22}=R_1-\mathrm{i}R_1\phi_2x_2\ b_{22}=-\rho_{22}\omega^2+\mathrm{i}\omega b_1,\\
&a_{23}=-\mathrm{i}R_1\phi_2x_3\ b_{23}=0,\\
&a_{31}=Q_2+\mathrm{i}R_2\phi_1x_1\ b_{31}=-\rho_{13}\omega^2-\mathrm{i}\omega b_2,\\
&a_{32}=\mathrm{i}R_2\phi_1x_2\ b_{32}=0,\\
&a_{33}=R_2+\mathrm{i}R_2\phi_1x_3\ b_{33}=-\rho_{33}\omega^2+\mathrm{i}\omega b_2,
\end{aligned} \tag{A-2}$$

and:

$$\begin{aligned}
x_1&=\mathrm{i}(\phi_2Q_1-\phi_1Q_2)/Z,\\
x_2&=\mathrm{i}\phi_2R_1/Z,\\
x_3&=-\mathrm{i}\phi_1R_2/Z,
\end{aligned} \tag{A-3}$$

$$Z=\frac{\mathrm{i}\omega\eta\phi_1^2\phi_2\phi_{20}R_0^2}{3\kappa_1}-\frac{\rho_f\omega^2R_0^2\phi_1^2\phi_2\phi_{20}}{3\phi_{10}}-(\phi_2^2R_1+\phi_1^2R_2), \tag{A-4}$$

where ϕ_1 and ϕ_2 are the absolute porosities ($\phi_1+\phi_2=\phi$), $\phi_1=v_1\phi_{10}$ and $\phi_2=v_2\phi_{20}$. ϕ_{10} and ϕ_{20} are the local porosities of the host and inclusions, respectively, v_1 and v_2 are the volume ratios of the host medium and inclusions ($v_1+v_2=1$), respectively, and R_0 is the inclusion radius, and ω is angular frequency. The Biot dissipation coefficients (Biot 1956 and Ba et al. 2011) and the permeabilities of the two phases (Mavko et al. 2009) are as follows:

$$b_1=\phi_1\phi_{10}\frac{\eta_f}{\kappa_1},\ b_2=\phi_2\phi_{20}\frac{\eta_f}{\kappa_2}, \tag{A-5}$$

$$\kappa_1=\frac{\kappa_0\phi_1^3}{1-\phi_1^2},\ \kappa_2=\frac{\kappa_0\phi_2^3}{1-\phi_2^2}, \tag{A-6}$$

where $\kappa_0=25$ mD. The stiffness and density coefficients are as follows:

$$A=(1-\phi)K_s-\frac{2}{3}N-\frac{K_s}{K_f}(Q_1+Q_2),\ N=\mu_b, \tag{A-7}$$

$$Q_1=\frac{\phi_1\beta K_s}{\beta+\gamma},\ Q_2=\frac{\phi_2K_s}{1+\gamma}, \tag{A-8}$$

$$R_1=\frac{\phi_1 K_f}{\beta/\gamma+1},\ R_2=\frac{\phi_2 K_f}{1+1/\gamma}, \tag{A-9}$$

$$\gamma=\frac{K_s}{K_f}\frac{\phi_1\beta+\phi_2}{(1-\phi)-K_b/K_s}, \tag{A-10}$$

$$\rho_{00}=(1-\phi)\rho_s-\frac{1}{2}(\phi-1)\rho_f, \tag{A-11}$$

$$\rho_{01}=\frac{1}{2}(\phi_1-v_1)\rho_f,\ \rho_{02}=\frac{1}{2}(\phi_2-v_2)\rho_f, \tag{A-12}$$

$$\rho_{11}=\frac{1}{2}(\phi_1+v_1)\rho_f,\rho_{22}=\frac{1}{2}(\phi_2+v_2)\rho_f, \tag{A-13}$$

where K_s and K_f comprise the bulk moduli of minerals and fluid, respectively, K_b and μ_b are the bulk and shear moduli of the frame (obtained with the DEM equations), respectively, ρ_s and ρ_f represent the densities corresponding to the mineral mixture and fluid, respectively, and:

$$\beta=\frac{Q_1R_2}{Q_2R_1}=\frac{\phi_{20}}{\phi_{10}}\left[\frac{1-(1-\phi_{10})K_s/K_{b1}}{1-(1-\phi_{20})K_s/K_{b2}}\right], \tag{A-14}$$

where K_{b1} and K_{b2} correspond to the bulk moduli of the host and crack inclusions, which are computed by adding stiff and soft pores (with different aspect ratios) by the DEM equations, respectively.

Acknowledgements This work is supported by the Fundamental Research Funds for the Central Universities (B240201131) and the National Natural Science Foundation of China (grant no. 41974123, 42174161).

Declarations

Conflict of interest The authors declare that they have no known competing financial interests or personal relationships that could have appeared to influence the work reported in this paper.

References

Ablimiti Y, He W, Li N, Ma D, Liu H, Bian B, Ding X, Jiang M, Wang J, Cao J (2022) Mechanisms of deep oil–gas accumulation: new insights from the carboniferous central depression, Junggar Basin, China. Front Earth Sci 10:987822. https://doi.org/10.3389/feart.2022.987822

Alqahtani NJ, Chung T, Wang YD, Armstrong RT, Swietojanski P, Mostaghimi P (2021) Flow-based characterization of digital rock images using deep learning. SPE J 26:1800–1811

Andrä H, Combaret N, Dvorkin J, Glatt E, Han J, Kabel M, Keehm Y, Krzikalla F, Lee M, Madonna C, Marsh M, Mukerji T, Saenger EH, Sain R, Saxena N, Ricker S, Wiegmann A, Zhan X (2013) Digital rock physics benchmarks—part I: Imaging and segmentation. Comput Geosci 50:25–32. https://doi.org/10.1016/j.cageo.2012.09.005

Ba J, Carcione JM, Nie J (2011) Biot-rayleigh theory of wave propagation in double-porosity media. J Geophys Res 116:B06202. https://doi.org/10.1029/2010JB008185

Ba J, Cao H, Carcione J, Tang G, Yan X, Sun W, Nie J (2013) Multiscale rock-physics templates for gas detection in carbonate reservoirs. J Appl Geophys 93:77–82

Ba J, Xu W, Fu L, Carcione J, Zhang L (2017) Rock anelasticity due to patchy-saturation and fabric heterogeneity: a double-double porosity model of wave propagation. J Geophy Res Solid Earth 122(3):1949–1976. https://doi.org/10.1002/2016JB013882

Berryman JG (1992) Single-scattering approximations for coefficients in Biot's equations of poroelasticity. Acoust Soc Am J 91(2):551–571

Biot MA (1956) Theory of propagation of elastic waves in a saturated porous solid, I, low-frequency range. J Acoust Soc Am 28:168–178

Bultreys T, Van Offenwert S, Goethals W, Boone MN, Aelterman J, Cnudde V (2022) X-ray tomographic micro-particle velocimetry in porous media. Phys Fluids 34(4):042008

Carcione JM (2022) Anisotropic anelastic media. Wave Fields in Real Media. Elsevier, Amsterdam, pp 195–257. https://doi.org/10.1016/B978-0-32-398343-3.00013-1

Carcione JM, Avseth P (2015) Rock-physics templates for clay-rich source rocks. Geophysics 80(5):D481–D500

Carcione JM, Helle HB, Pham NH (2003) White's model for wave propagation in partially saturated rocks: comparison with poroelastic numerical experi-ments. Geophysics 68:1389–1398

Chapman M (2003) Frequency-dependent anisotropy due to meso-scale fractures in the presence of equant porosity. Geophys Prospect 51(5):369–379

David EC, Zimmerman RW (2012) Pore structure model for elastic wave velocities in fluid-saturated sandstones. J Geophys Res: Solid Earth 117:B07210. https://doi.org/10.1029/2012JB009195

Dvorkin J, Nur A (1993) Dynamic poroelasticity: a unified model with the squirt and the biot mechanisms. Geophysics 58(4):524–533

Ghasemi S, Khamehchiyan M, Taheri A, Nikudel MR, Zalooli A (2020) Crack evolution in damage stress thresholds in different minerals of granite rock. Rock Mech Rock Eng 53(3):1163–1178

Golikov P, Avseth P, Stovas A, Bachrach R (2012) Rock physics interpretation of heterogeneous and anisotropic turbidite reservoirs. Geophys Prospect 61(2):448–457

Guo J, Gurevich B (2020a) Frequency-dependent *P*-wave anisotropy due to wave-induced fluid flow and elastic scattering in a fluid-saturated porous medium with aligned fractures. J Geophys Res: Solid Earth 125:e2020JB02320

Guo J, Gurevich B (2020b) Effects of coupling between wave-induced fluid flow and elastic scattering on *P*-wave dispersion and attenuation in rocks with aligned fractures. J Geophys Res: Solid Earth 125:e2019JB018685

Guo M, Fu L, Ba J (2009) Comparison of stress-associated coda attenuation and intrinsic attenuation from ultrasonic measurements. Geophys J Int 178:447–456

Gupta SD, Chatterjee R, Farooqui MY (2012) Rock physics template (RPT) analysis of well logs and seismic data for lithology and fluid classification in Cambay Basin. Int J Earth Sci 101(5):1407–1426

Gurevich B, Makarynska D, de Paula OB, Pervukhina M (2010) A simple model for squirt-flow dispersion and attenuation in fluid-saturated granular rocks. Geophys 75(6):N109–N120

Jangda Z, Menke H, Busch A, Geiger S, Bultreys T, Lewis H, Singh K (2023) Pore-scale visualization of hydrogen storage in a sandstone at subsurface pressure and temperature conditions: trapping, dissolution and wettability. J Colloid Interface Sci 629:316–325

Jun J, Xian B, Lian L, Chen S, Wang J, Li J (2023) Reformation of deep clastic reservoirs with different diagenetic intensities by microfractures during late rapid deep burial: Implications from diagenetic physical simulation of Cretaceous Qingshuihe formation in the southern margin of Junggar Basin NW China. Pet Explor Dev 50(2):346–359

Kadyrov R, Nurgaliev D, Saenger EH, Balcewicz M, Minebaev R, Statsenko E, Galiullin B (2022) Digital rock physics: defining the reservoir properties on drill cuttings. J Petrol Sci Eng 210:110063

Kobayashi Y, Mavko G (2016) Variation in *P*-wave modulus with frequency and water saturation: extension of dynamic-equivalent-medium approach. Geophys 81(5):D479–D494

Kumar S, Mendhe VA, Kamble AD, Varma AK, Mishra DK, Bannerjee M, Prasad AK (2019) Geochemical attributes, pore structures and fractal characteristics of Barakar shale deposits of Mand-Raigarh Basin, India. Mar Pet Geol 103:377–396

Li S, Wang W, Su Y, Guo J, Tang X (2024) P- and SV-wave dispersion and attenuation in saturated microcracked porous rock with aligned penny-shaped fractures. Pet Sci 21:143–161

Luo C, Ba J, Guo Q (2023) Probabilistic seismic petrophysical inversion with statistical double-porosity Biot-Rayleigh model. Geophysics 88(3):M157–M171

Madonna C, Quintal B, Frehner M, Almqvist BS, Tisato N, Pistone M, Saenger EH (2013) Synchrotron-based X-ray tomographic microscopy for rock physics investigations synchrotron-based rock images. Geophys 78(1):D53–D64

Mavko G, Mukerji T, Dvorkin J (2009) The rock physics handbook: tools for seismic analysis of porous media. Cambridge University Press, Cambridge

Menke HP, Maes J, Geiger S (2021) Upscaling the porosity–permeability relationship of a microporous carbonate for darcy-scale flow with machine learning. Sci Rep 11:2625. https://doi.org/10.1038/s41598-021-82029-2

Mori T, Tanaka K (1973) Average stress in matrix and average elastic energy of materials with misfitting inclusions. Acta Metall 21:571–574

Okabe H, Blunt MJ (2004) Prediction of permeability for porous media reconstructed using multiple-point statistics. Phys Rev E: Stat, Nonlin, Soft Matter Phys 70(2):066135

Pang M, Ba J, Carcione J, Picotti S, Zhou J, Jiang R (2019) Estimation of porosity and fluid saturation in carbonates from rock-physics templates based on seismic Q. Geophys 84(6):M25–M36. https://doi.org/10.1190/geo2019-0031.1

Pang M, Ba J, Fu L, Carcione JM, Markus UI, Zhang L (2020) Estimation of microfracture porosity in deep carbonate reservoirs based on 3D rock-physics templates. Interpretation 8(4):SP43–SP52

Pang M, Ba J, Carcione J, Zhang L, Ma R, Wei Y (2021) Seismic identification of tight-oil reservoirs by using 3D rock-physics templates. J Pet Sci Eng 201:108476

Pang M, Ba J, Carcione JM, Balcewicz M, Yue W, Saenger EH (2022) Acoustic and electrical properties of tight rocks: a comparative study between experiment and theory. Surv Geophys 43:1–31

Pang M, Ba J, Carcione JM, Saenger EH (2024a) Combined acoustical-electrical modeling for tight sandstones verified by laboratory measurements. Int J Rock Mech Min Sci 176:105682

Pang M, Balcewicz M, Ba J, Carcione JM, Siegert M, Saenger E (2024b) Acoustical-electrical models of tight rocks based on digital rock physics and double-porosity theory. Geoenergy Sci Eng 235:212634

Paustian R, Andersson L, Helland JO, Wildenschild D (2021) On the relationship between capillary pressure, saturation, and interfacial area for three-phase flow in water-wet porous media. Adv Water Resour 151:103905

Pride SR, Berryman JG (2003) Linear dynamics of double-porosity and dual-permeability materials Part 1: governing equations and acoustic attenuation. Phys Rev E 68:036603

Qi H, Ba J, Müller TM (2021) Temperature effect on the velocity-porosity relationship in rocks. J Geophys Res: Solid Earth 126(1):e2019JB019317. https://doi.org/10.1029/2019JB019317

Qu H, Yan Z, Zheng C, Xu W, He F, Sun Q, Zhang X, Li M (2023) Quantitative characterization and origin of differences in pore parameter distribution: a case study of the lower cambrian longwangmiao formation in the gaoshiti area of central Sichuan Basin. Front Earth Sci 10:1043148

Saenger EH, Shapiro SA, Keehm Y (2005) Seismic effects of viscous biot-coupling: finite difference simulations on micro-scale. Geophys Res Lett 321(14):337–349

Saenger EH, Vialle S, Lebedev M, Uribe D, Osorno M, Duda M, Steeb H (2016) Digital carbonate rock physics. Solid Earth 7:1185–1197. https://doi.org/10.5194/se-7-1185-2016

Sakhaee-Pour A, Bryant SL (2014) Effect of pore structure on the producibility of tight-gas sandstones. AAPG Bull 98:663–694

Saxena N, Hofmann R, Hows A, Saenger EH, Duranti L, Stefani J, Wiegmann A, Kerimov A, Kabel M (2019) Rock compressibility from microcomputed tomography images: controls on digital rock simulations. Geophysics 84:W127–W139

Schlüter S, Sheppard A, Brown K, Wildenschild D (2014) Image processing of multiphase images obtained via x-ray microtomography: a review. Water Resour Res 50:3615–3639. https://doi.org/10.1002/2014WR015256

Siegert M, Gurris M, Lebedev M, Saenger EH (2022) Numerical modeling of the permeability in Bentheim sandstone under confining pressure. Geophys. https://doi.org/10.1190/geo2021-07181

Solano NA, Soroush M, Clarkson CR, Krause FF, Jensen JL (2017) Modeling core-scale permeability anisotropy in highly bioturbated "tight oil" reservoir rocks. Comput Geosci 21(3):567–593

Song Y, Hu H, Rudnicki JW (2016) Dynamic bulk and shear moduli due to grain-scale local fluid flow in fluid-saturated cracked poroelastic rocks: theoretical model. J Mech Phys Solids 92:28–54

Spurin C, Armstrong RT, McClure J, Berg S (2023) Dynamic mode decomposition for analysing multi-phase flow in porous media. Adv Water Resour 175:104423

Sun H, Duan L, Liu L, Fan W, Fan D, Yao J, Zhao J (2019) The influence of micro-fractures on the flow in tight oil reservoirs based on pore-network models. Energies 12(21):4104

Tan W, Ba J, Muller T, Fang G, Zhao H (2020) Rock physics model of tight oil siltstone for seismic prediction of brittleness. Geophys Prospect 68(5):1554–1574

Tang X (2011) A unified theory for elastic wave propagation through porous media containing cracks-an extension of biot's poroelastic wave theory. Sci China Earth Sci 54:1441–1452

Toksöz MN, Johnston HD, Timur A (1979) Attenuation of seismic waves in dry and saturated rocks: i laboratory measurements. Geophysics 44(4):681–690. https://doi.org/10.1190/1.1440969

Vogelaar B, Smeulders D, Harris J (2010) Exact expression for the effective acoustics of patchy-saturated rocks. Geophysics 75(4):N87–N96

Wang E, Liu G, Pang X, Li C, Wu Z (2020) Diagenetic evolution and formation mechanisms of middle to deep clastic reservoirs in the Nanpu sag Bohai Bay Basin, East China. Pet Explor Dev 47(2):343–356

Wang S, Tan M, Wang X, Zhang L (2022) Microscopic response mechanism of electrical properties and saturation model establishment in fractured carbonate rocks. J Petrol Sci Eng 208:109429

White JE (1975) Computed seismic speeds and attenuation in rocks with partial gas saturation. Geophysics 40:224–232. https://doi.org/10.1190/1.1440520

Wildenschild D, Vaz CMP, Rivers ML, Rikard D, Christensen BSB (2002) Using x-ray computed tomography in hydrology: systems, resolutions, and limitations. J Hydrol 267:285–297. https://doi.org/10.1016/S0022-1694(02)00157-9

Zhang L, Ba J, Fu L, Carcione JM, Cao C (2019) Estimation of pore microstructure by using the static and dynamic moduli. Int J Rock Mech Min Sci 113:24–30. https://doi.org/10.1016/j.ijrmms.2018.11.005

Zhang L, Ba J, Carcione JM (2021) Wave propagation in infinituple-porosity media. J Geophy Res: Solid Earth 126(4):e2020JB021266

Zhang L, Ba J, Carcione JM (2022) Seismic wave propagation in partially saturated rocks with a fractal distribution of fluid-patch size. J Geophys Res: Solid Earth 127(2):e2021JB023809

Zhou J, Xu C, Yao G, Yang G, Zhang J, Hao Y, Wang F, Pan L, Gu M, Li W (2015) Genesis and evolution of Lower Cambrian Longwangmiao Formation reservoirs Sichuan Basin, SW China. Pet Explor Dev 42(2):175–184

Zhou S, Yan G, Xue H, Guo W, Li X (2016) 2D and 3D nanopore characterization of gas shale in Longmaxi formation based on FIB-SEM. Mar Pet Geol 73:174–180

Zou C, Hou L, Hu S, Zhu R, Liu S, Yang Z, Gu Z, Fan Y, Yang C (2014) Prospect of ultra-deep petroleum onshore China. Energy Explor Exploit 32:19–40. https://doi.org/10.1260/0144-5987.32.1.19